

# E2 temperature and Gamma distribution of polygonal planar tessellations

Ran Li<sup>1</sup>, Consuelo Ibar<sup>2</sup>, Zhenru Zhou<sup>2</sup>, Kenneth D. Irvine<sup>2\*</sup>, Liping Liu<sup>1,3†</sup>, and Hao Lin<sup>1‡</sup>

February 27, 2020

1. Department of Mechanical and Aerospace Engineering, Rutgers, The State University of New Jersey
2. Waksman Institute and Department of Molecular Biology and Biochemistry, Rutgers, The State University of New Jersey
3. Department of Mathematics, Rutgers, The State University of New Jersey

## Abstract

From Bénard-Marangoni convection to salt flat in Bolivia, from veins on leaves to cells on *Drosophila* wing discs, polygon-based networks exhibit great complexities, yet similarities persist and statistical distributions can be remarkably consistent. Here based on analysis of 117 data sets from random polygonal tessellations of a wide variety of physical origins, we demonstrate the ubiquity of an exponential, Boltzmann-like distribution in the squared norm of the deformation tensor. This distribution directly leads to a Gamma distribution in polygon aspect ratio under a monotonic mapping, and enables the definition of a pseudo temperature - the E2 temperature - that varies by nearly two orders of magnitude across the systems. Data examined in the phase space of this temperature and the mean normalized perimeter exhibit defined correlations and regimes, suggesting different “phases” based only on geometric quantifiers for broad classes of phenomena.

Polygonal networks are one of nature’s favorite ways of organizing the multitude - from Bénard-Marangoni convection in a laboratory [14] to supergranulation on the solar surface [37]; from ice wedges in northern Canada [71] to the scenic Salar de Uyuni in Bolivia [31]; and from veins on leaves [16] to cells on *Drosophila* wing discs [62] (Fig. 1). These systems are driven by distinctive physical mechanisms, yet they share common features. Individual constituents, namely, “cells” appear to “randomize” into statistical distributions, and only interact with their immediate neighbors. On the collective level, especially in the dynamic and active systems, rich phenomena are observed, including unjamming and jamming, fluid-to-solid phase transition, and flow and migration [9, 25, 30, 41, 49, 59, 64, 73, 80].

Despite the complexity and variabilities involved in these phenomena, similarity patterns emerge. One particularly interesting instance is provided recently by Atia *et al.* [3]. Within the context of confluent biological tissue and based on extensive experiments both *in vitro* and *in vivo*, the authors found that data

---

\*Corresponding email: irvine@waksman.rutgers.edu

†Corresponding email: liu.liping@rutgers.edu

‡Corresponding email: hlin@soe.rutgers.edu

on cell aspect ratio collapse and follow a normalized Gamma distribution, implying a universal principle underlying the geometric configuration and pertinent processes.

What is the basis of this universality? Does it carry beyond the biological context? In this work we analyze a total of 117 data sets in 11 groups that include convection patterns (Bénard and solar supergranulation), landforms (salt flats, on Mars, and in or near the Arctic), cracked dry earth, biological patterns (veins on leaves, cells on *Drosophila* wing discs observed via two separate approaches, and plated MDCK cells), and granular assembly (Fig. 1 and Table 1). We demonstrate that the Gamma distribution in polygonal aspect ratio arises from an exponential, Boltzmann-like distribution in the squared mean-field strain tensor norm, based on which we develop a unifying solution. Furthermore, both distributions persist in all data examined, and hence are true, general characteristics of random polygonal tessellations. Importantly, the exponential distribution naturally gives rise to a pseudo-temperature consistent with the canonical form of Edwards measure [5, 23, 24, 54]. We term this temperature the “E2 temperature”. A phase space is formed in conjunction with the mean normalized perimeter, which exhibits distinctive correlations and regimes suggesting “phases”. A threshold value identified in the specific context of confluent biological tissue modeling [9] carries over to demarcate phase boundaries in a much broader sense. Overall these geometric quantifiers transcend the specific systems, promise a framework to understand a wide class of phenomena, and can be generalized to higher dimensions although only planar tessellations are examined in the current work.

## Theory

We begin by a theoretical construction defining the mean-field deformation tensor and connecting its statistics with that of the aspect ratio. An exemplary processed image of a *Drosophila* wing disc 120h after egg laying (AEL) is shown in Figure 1j, where the color scale indicates magnitude of the cell aspect ratio (defined in Methods). We choose as our reference frame a *regular*  $n$ -polygon centered at the origin, with vertices

$$\mathbf{x}_j = [\cos(j2\pi/n), \sin(j2\pi/n)], \quad j = 1, \dots, n. \quad (1)$$

This polygon, denoted by  $\mathcal{P}_R$ , has an area of  $A_0 = (n/2) \sin(2\pi/n)$ , a perimeter of  $L_0 = 2n \sin(\pi/n)$ . Figure 1k uses  $n = 6$ , a hexagon as an illustrative example. We consequently regard any  $n$ -sided polygon  $\mathcal{P}$  with vertices  $\mathbf{y}_j$  as a “deformation” from  $\mathcal{P}_R$ ,

$$\mathbf{y}_j = \mathbf{x}_j + \mathbf{u}_j, \quad j = 1, \dots, n. \quad (2)$$

Note that this deformation is to be understood as a morphological deviation from the reference  $\mathcal{P}_R$ , rather than an actual physical deformation, although the latter is a possibility. We also require that the centroid of  $\mathcal{P}$  is aligned with that of  $\mathcal{P}_R$ . The deformation is in general non-uniform, in the sense that for  $n \geq 3$ , a single deformation tensor of  $\mathbf{F} \in \mathbb{R}^{2 \times 2}$  cannot be identified by  $\mathbf{y}_j = \mathbf{F}\mathbf{x}_j$  for all of  $j = 1, \dots, n$ . Nevertheless we *can* introduce an approximation, namely,

$$\mathbf{y}_j \approx \mathbf{y}'_j = \mathbf{F}\mathbf{x}_j, \quad j = 1, \dots, n. \quad (3)$$

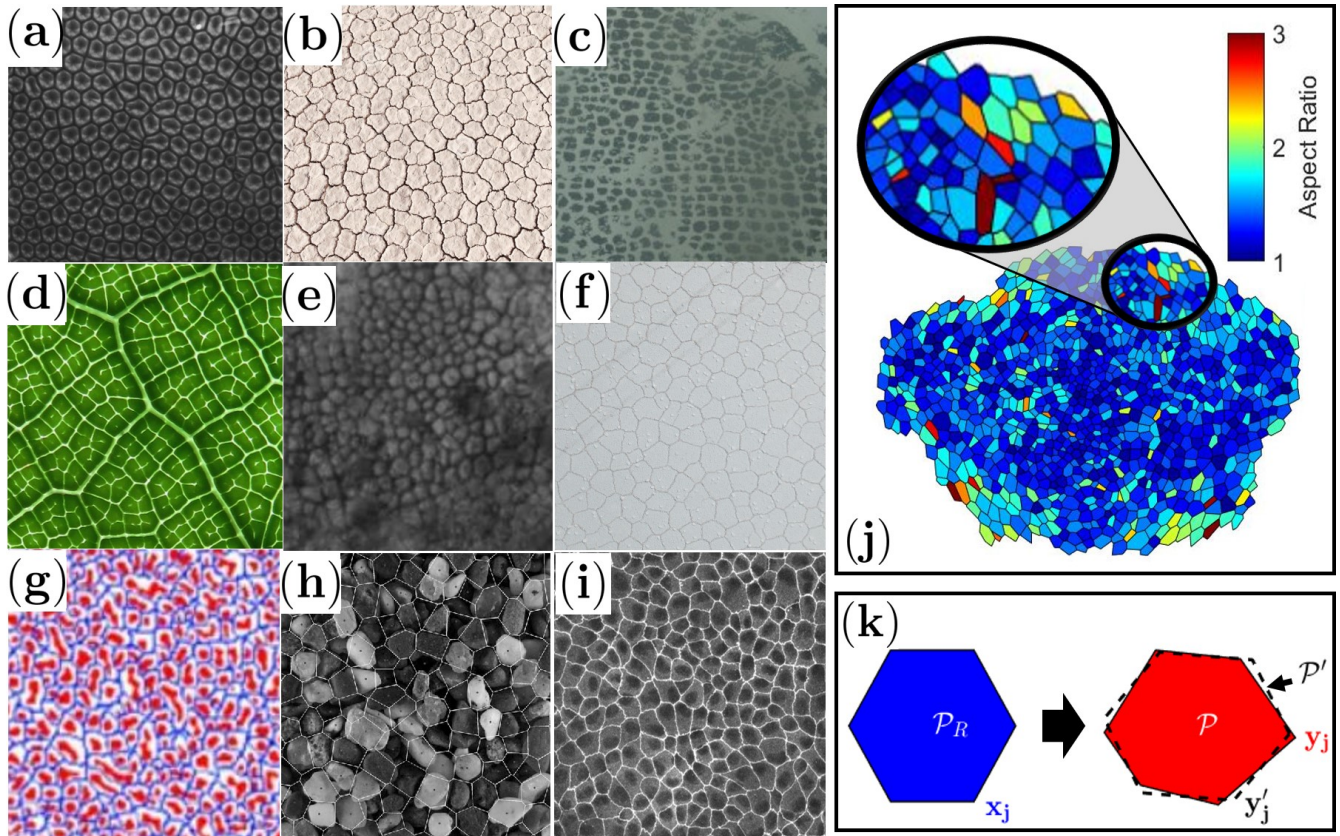


Figure 1: (a)-(i) Examples of randomized polygonal networks in nature. (a) Bénard-Marangoni convection cells [14]; (b) Land cracks due to desiccation [43]; (c) Ice wedges from northern Canada [71]; (d) Veins on a *Ficus lyrata* leaf [16]; (e) Desiccation pattern of an ancient lake on Mars [50]; (f) A snapshot of Salar de Uyuni in Bolivia, world's largest salt flat [31]; (g) Supergranulation on solar surface [37]; (h) A granular assembly: the surface of a well-sorted sand and the polygons are the Voronoi volumes [12]; (i) Plated MDCK cells (this work). (j) A processed image of a developing *Drosophila* wing disc (this work) with the aspect ratio of cells color-mapped. (k) A regular hexagon  $\mathcal{P}_R$  (blue, with vertices  $\mathbf{x}_j$ ), a deformed hexagon  $\mathcal{P}$  (red, with vertices  $\mathbf{y}_j$ ), and a uniform deformation as mean-field approximation  $\mathcal{P}'$  (black dashed outline, with vertices  $\mathbf{y}'_j$ ).

This approximation is analogous to a Taylor expansion in which only the leading order term is retained. Different approaches can be used to obtain  $\mathbf{F}$ , for example, by minimizing the difference between  $\mathbf{y}_j$  and  $\mathbf{F}\mathbf{x}_j$  for all  $j$  in the sense of least-square for an over-determined problem. The use of a uniform deformation to approximate the local and non-uniform deformation field is effectively coarse-graining, reducing the degree of freedom from  $2n$  to 4 and suppressing the fluctuations.  $\mathbf{F}$  can thus be regarded as a mean-field state variable that characterizes the cellular microstate. This idea is illustrated in Figure 1k (right), where  $\mathcal{P}'$  is the approximate and uniformly deformed polygon. From  $\mathbf{F}$  we define the usual strain tensor

$$\mathbf{E} = (\mathbf{F}^T \mathbf{F})^{\frac{1}{2}} - \mathbf{I} \approx \frac{1}{2}[(\mathbf{F} - \mathbf{I}) + (\mathbf{F} - \mathbf{I})^T], \quad (4)$$

where  $\mathbf{I}$  is the identity tensor, and the approximation is valid in the small-to-moderate deformation regime.

We next bring forth the main postulate, that the strain tensor  $\mathbf{E}$  characterizes a microstate and the cells follow a Boltzmann-type distribution,

$$P(\mathbf{E} | \text{Tr} \mathbf{E} = 0) \propto \exp(-\beta \psi(\mathbf{E})), \quad \psi := |\mathbf{E}|^2 = \text{Tr}(\mathbf{E}^T \mathbf{E}). \quad (5)$$

Here  $\psi$  is defined as the squared Frobenius norm of  $\mathbf{E}$  and will be treated as a pseudo-energy in our context. The trace-free constraint on  $\mathbf{E}$  restricts us to isochoric deformations (by always requiring that  $\mathcal{P}_R$  has the same area as  $\mathcal{P}$ ) and reduces the degree of freedom to 2. Experimental verification of this postulate is presented later. We demonstrate that Eq. (5) sufficiently gives rise to the  $k$ -Gamma distributions observed in experiments such as in [3]. The derivation is as follows. The aspect ratio  $a_r$  of the polygon, as calculated via the second area moments, is related to  $|\mathbf{E}|$  by (SI)

$$a_r^2 = 1 + g(\psi), \quad g(t) = 2t^2 + 4t + [(2t^2 + 4t + 1)^2 - 1]^{1/2}. \quad (6)$$

The cumulative distribution function with  $a_r \leq 1 + x$  is given by

$$F(x) \propto \int_{\Omega_{\mathbf{E}}} \exp(-\beta \psi(\mathbf{E})) d\mathbf{E}, \quad (7)$$

$$\Omega_{\mathbf{E}} = \{\mathbf{E} \in \mathbb{R}_{\text{sym}}^{2 \times 2} : \text{Tr} \mathbf{E} = 0, \sqrt{1 + g(\psi(\mathbf{E}))} - 1 \leq x\}. \quad (8)$$

Explicitly, we set  $\mathbf{E} = (u, v; v, -u)$ , so that  $\psi = 2(u^2 + v^2)$ . Carrying over the integration in (7) we have

$$F(x) = 1 - \exp(-\beta \zeta(x)), \quad \zeta(x) = g^{-1}(2x + x^2), \quad (9)$$

and subsequently the probability density function (PDF) for  $x$ ,

$$\rho(x) = F'(x) = \beta \zeta'(x) \exp(-\beta \zeta(x)). \quad (10)$$

Here we term  $x$  (defined as  $a_r - 1$ ) the ‘‘shape factor’’ [84]. Equation (10) is a main result of this paper.

A similar integration over the probability space reveals

$$\rho(\psi) = \beta \exp(-\beta \psi). \quad (11)$$

Type (abbreviation)	$M$	$N$	$R^2,  \mathbf{E} ^2$	$R^2, a_r - 1$
Bénard-Marangoni Convection (Bénard)	9	163 – 370	$0.989 \pm 0.0111$	$0.966 \pm 0.0175$
Granular Packing (Gran-exp & Gran-sim)	11	279 – 2216	$0.986 \pm 0.0139$	$0.947 \pm 0.0442$
Salt Flat of Uyuni (Salt Flat)	7	193 – 849	$0.993 \pm 0.0056$	$0.970 \pm 0.0185$
Landforms on Mars (Mars)	9	219 – 5826	$0.981 \pm 0.0162$	$0.919 \pm 0.0713$
Veins on Leaves (Leaves)	6	338 – 6050	$0.988 \pm 0.0107$	$0.946 \pm 0.0511$
Landforms in the Arctic (Arctic)	10	104 – 1061	$0.918 \pm 0.0793$	$0.914 \pm 0.0724$
Supergranulation on Solar Surface (Solar)	8	192 – 1645	$0.980 \pm 0.0163$	$0.939 \pm 0.0509$
Cracked Dry Earth (Cracks)	9	298 – 1596	$0.978 \pm 0.0185$	$0.960 \pm 0.0277$
Drosophila Wing Disc, Fixed (Droso Fix)	33	938 – 4205	$0.997 \pm 0.0026$	$0.984 \pm 0.0114$
Drosophila Wing Disc, Live (Droso Live)	10	902 – 1231	$1.000 \pm 6.19 \times 10^{-4}$	$0.987 \pm 0.0067$
Plated MDCK Cells (MDCK)	5	553 – 2283	$0.996 \pm 0.0045$	$0.978 \pm 0.022$

Table 1: Summary of data: abbreviations are defined within parenthesis and are used in figure legends;  $M$  indicates number of data sets in each type;  $N$ , the number of cells in each set (range only).  $R^2$  for  $|\mathbf{E}|^2$  indicates quality of fitting (e.g., in left column, Fig. 2);  $R^2$  for  $a_r - 1$  indicates quality of agreement between theory and data (e.g., in middle column, Fig. 2). For Granular Packing the Voronoi volumes are analyzed, and data include both experimental (Gran-exp) and numerical (Gran-sim) studies. Data sources are indicated in Methods. The total number of data sets presented is 117.

Note the difference in the arguments in (5) (tensor) and (11) (scalar). We realize that for the two scalars  $a_r$  and  $\psi$ , Eq. (6) defines a monotonic, one-to-one mapping that can be used for probability transformation: given the distribution of one, the other can be determined (SI). Furthermore, deriving from the tensor distribution, the scalar variable  $\psi$  also follows a Boltzmann distribution because configuration density function  $\Omega(\psi)$  is constant in the two-dimensions. This function, however, is in general not constant in higher dimensions, as discussed below.

## Experimental data validate $|\mathbf{E}|^2$ and $a_r$ distributions

The postulate and results are extensively validated with a total of 117 data sets spanning 11 groups summarized in Table 1; detailed descriptions, data sources, and method of analysis are presented in the Methods section. Fig. 2 uses 5 representative cases to demonstrate the agreement. (6 more are shown in Fig. S2 in the SI.)

The left column shows the PDFs of  $|\mathbf{E}|^2$ , which are very well fitted by the exponential form,  $\exp(-\beta|\mathbf{E}|^2)$ . Extracted  $\beta$ , via a least-square fitting approach, spans nearly two orders of magnitude. In all data sets analyzed, the minimum is  $\beta = 3.57$ , corresponding to a Drosophila wing disc in an early stage of development (84h AEL, Fig. 2m); the maximum is  $\beta = 157$ , corresponding to a case of Bénard-Marangoni convection.

The center column shows the PDFs of the shape factor,  $a_r - 1$  (symbols). The theoretical predictions per Eq. (10) are shown in dashed, and exhibit excellent agreement with data. They are generated per Eq. (10), with the single input parameter,  $\beta$ , extracted from the analysis of  $|\mathbf{E}|^2$  distribution.

Lastly in the right column, the PDFs for  $a_r - 1$  are normalized with  $\langle a_r \rangle - 1$ , where  $\langle \cdot \rangle$  denotes the mean:

$$\langle x \rangle = \int_0^\infty x \rho(x) dx. \quad (12)$$

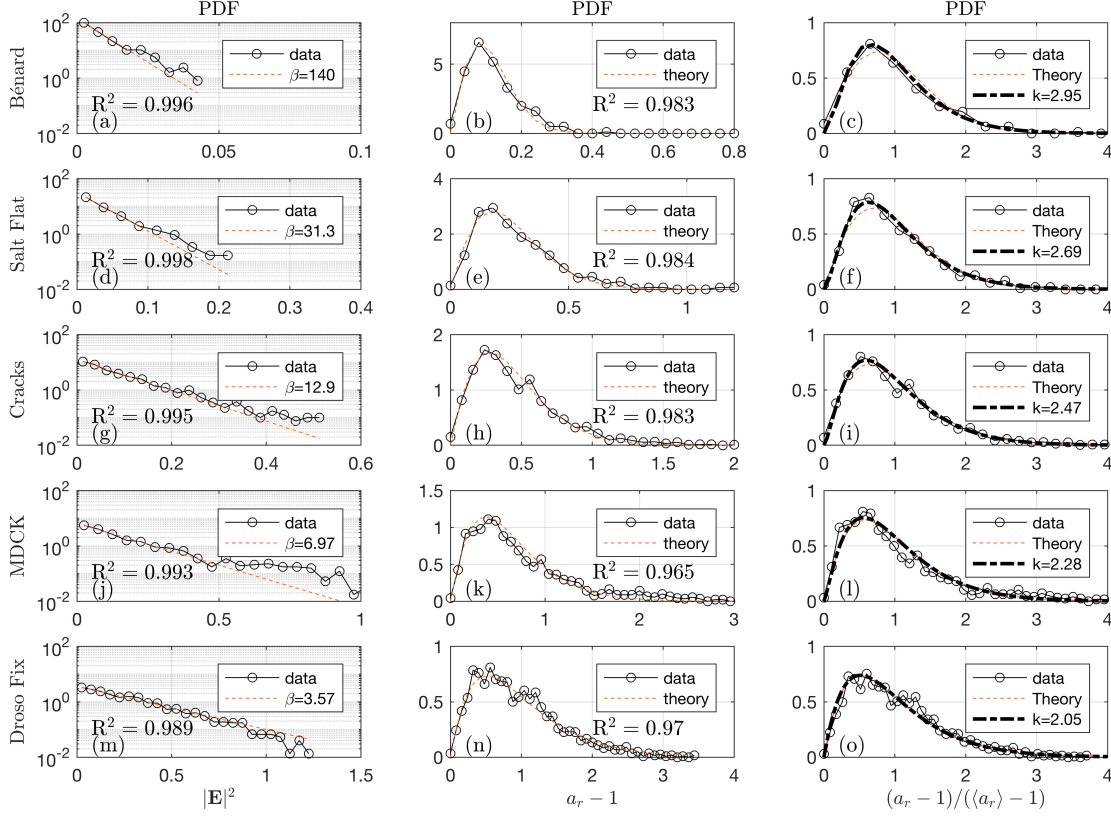


Figure 2: Universality in strain and aspect ratio distributions. Left column shows the PDFs of  $|\mathbf{E}|^2$ , fitted with an exponential form  $\exp(-\beta|\mathbf{E}|^2)$  to extract  $\beta$ . This  $\beta$  value is used in Eq. (10) to generate the theoretical curves in the middle column (dash), in comparison to the aspect ratio data (symbols). The coefficients of determination,  $R^2$  are shown within the panels. Right column: both data and theoretical curves from the center column are normalized using the mean values, and fitted with a  $k$ -Gamma function (13) (thick dashed). A single parameter  $k$  is extracted and shown in the figure legends. Data are from [74], [28], and [70], respectively, for the top 3 rows; and from this work for MDCK and Drosophila.

Both data and theoretical predictions are normalized following this practice. The dot-dashed are best fits using a  $k$ -Gamma distribution defined as

$$\rho_{kG}(x_1; k) = \frac{k^k}{\Gamma(k)} x_1^{k-1} \exp(-kx_1), \quad (13)$$

where  $\Gamma(k)$  is the Gamma function, and  $k$  is the single fitting parameter. The agreement is evident, and the  $k$ -values are found to vary between 2 and 3.

Overall corroboration between theory and data are quantified by the coefficient of determination,  $R^2$ , and are listed in Table 1 for all cases studied. (See Methods for definition.) The values are uniformly close to 1 (“perfect agreement”) with minimal variations from case to case. Note that the visible deviation in the “tails” of the PDFs for  $|\mathbf{E}|^2$  become invisible if the results are shown instead on a linear scale. Validity of the theoretical prediction (10) is also attested by Fig. 3a. Here we define a pseudo temperature  $T$  as the inverse of  $\beta$ , namely,  $T = \beta^{-1}$ . To compare with data, a theoretical prediction is generated by using

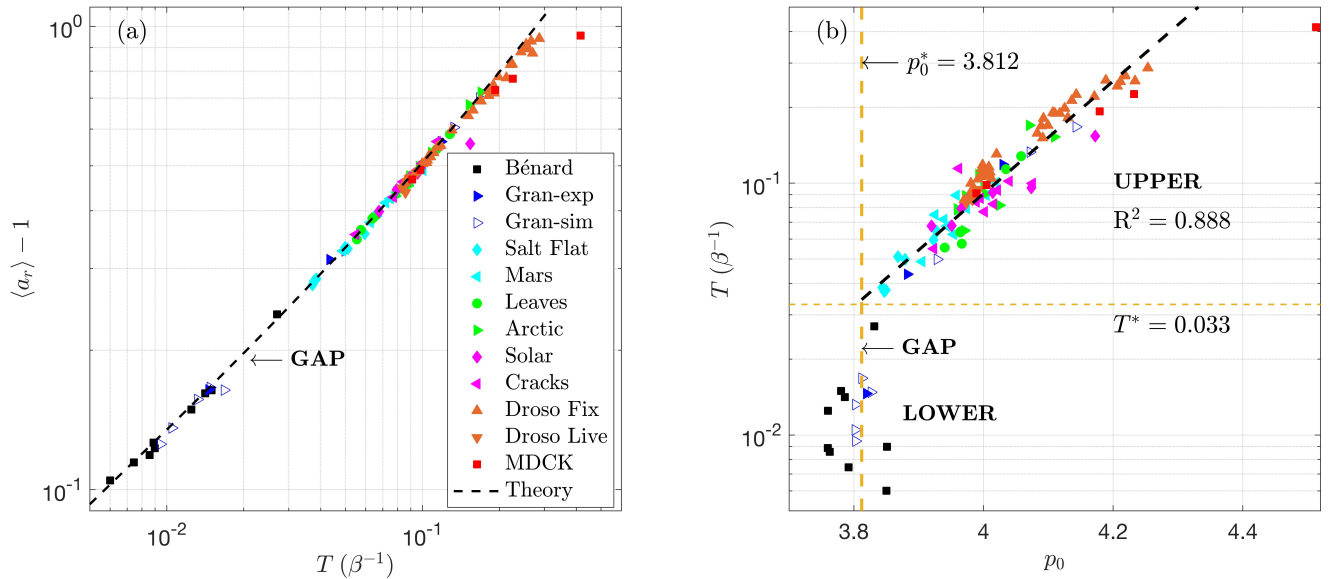


Figure 3: (a) Overall correlation between  $a_r$  and  $T (\beta^{-1})$  for all data sets analyzed (symbols); the theoretical prediction (dashed) is generated per (10). (b) A geometric phase space in terms of  $T$  and  $p_0$ . Symbols follow the same definition as in (a).

(10) in the integration (12).

The above results validate that the strain tensor norm does follow an exponential, Boltzmann-like distribution. (The slightly different form (5) is validated, too, by simply considering isotropy of  $\mathbf{E}$ ; see SI.) The universality of this distribution in all data sets, according to our theory, necessarily leads to a universality of  $k$ -Gamma distributions for the aspect ratio. That is, the validity extends beyond the confluent tissues studied in [3], and to all systems we analyzed. As a corollary, (10) provides a fundamental solution for the aspect ratio, of which the  $k$ -Gamma distributions (13) are convenient approximations. This solution does not normalize to a single curve with a single  $k$  value if fitted with Gamma distributions. In fact, it predicts a positive correlation between  $\beta$  and  $k$  (SI). Qualitatively, this means that PDFs of aspect ratio ( $a_r$ , or equivalently,  $x$ ) with wider spread and greater mean (corresponding to lower values of  $\beta$ ) present themselves relatively to the left after normalization (corresponding to lower values of  $k$  and noting that maxima occur at  $1 - 1/k$  per (13)). This trend is fully corroborated with data from our own work (Fig. 2, and Fig. S2 in SI, center and right columns) and Atia et al. [3] (Fig. 3 therein), as well as predictions from a self-propelled Voronoi model in the latter. In summary, the variability in  $k$  arises from the variability in  $\beta$ , the inverse temperature which is a fundamental quantity.

## A geometric phase space

Further intriguing patterns are revealed in Fig. 3b when  $T$  is plotted against  $p_0$ , the target shape index, or a preferred, area-normalized perimeter [9]. Here  $p_0 = L/\sqrt{A}$ , where  $L$  is the polygon perimeter, and  $A$  is area. For each data set,  $p_0$  is the mean value of all polygons therein. Note that both  $p_0$  and  $T$  are purely geometrically derived - the strain tensor is computed from shape deformation. Immediately we note that data is divided into two regimes. The upper regime is demarcated approximately by  $T^* = 0.033$  and  $p_0^* = 3.812$ . Here  $p_0^*$  is that of a regular pentagon, and is identified by [9] as the threshold for a

“solid-liquid” (rigidity) transition. Data in this regime has a pronounced trend: except for the apparent outlier (the single data point to the far upper-right of Fig. 3b), the rest follows approximately

$$p_0 \propto \ln T,$$

as indicated by the dashed line from best fitting. The coefficient of determination for the fitting is  $R^2 = 0.888$  for all data groups pooled together. The outlier corresponds to MDCK cells plated at  $1.5 \times 10^4$  cells/cm<sup>2</sup>, where cells have non-convex shapes with tortuous edges - see Fig. S1c in the SI, so that our approximation using straight-edged polygons may not be accurate. Further discussion on the above correlation is below. In contrast, data in the lower regime behave differently: they are characterized by lower temperature and  $p_0$  around the transitional value of  $p_0^*$  ( $3.76 < p_0 < 3.85$ ). Very peculiarly, all data from group Gran-sim (hollow triangles) in this regime gather around  $p_0^*$ . In addition, a “gap” appears to exist between  $T = 0.0168$  and  $0.033$ , between which only a single data point in the Bénard group exists. This gap is also evident in Fig. 3a. However, it remains unclear whether this is due to the finite size of data sets available.

We speculate that the regimes correspond to “phases”. Especially, the critical value in  $p_0$  occurs near  $p_0^*$ , the rigidity transition threshold proposed by Bi *et al.* [9]. In that work this threshold is deduced specific to a second-order, perimeter-based energy model suitable for biological tissues and alike. Data presented here include systems driven by drastically different physical mechanisms beyond the simple model, e.g., Bénard-Marangoni cells and solar supergranulation via natural convection; granular patterns from packing; salt flats and land cracks via desiccation; and various landforms via seasonal and geological forces. Yet  $p_0^*$  does seem to pose as a threshold demarcating regimes. On the other hand, the precise meaning of phases needs to be cautiously examined. In [9], the fluid-like regime of  $p_0 > p_0^*$  is defined by that the energy barrier for cell rearrangement (known as the T1 transition) practically vanishes, allowing “free flow” of cells. It is not clear if this concept can be generalized. A detailed study is needed and is the scope of future work. Nevertheless, the current result indicates that  $p_0^*$  does carry more universality which extends previously suggestions.

## E2 temperature and thermodynamic implications

We thus far presented data in terms of a pseudo temperature,  $T$ . Indeed, in the presence of Boltzmann-like distributions, the definition of such a temperature is straightforward and appropriate. Borrowing from the canonical form of Edwards measure in the context of granular assembly, and replacing volume with the squared tensor norm as pseudo energy, we have [18, 23, 24, 54],

$$\rho_{\text{Edw}}(\psi) = \frac{\Omega(\psi) \exp(-\beta\psi)}{Q}, \quad (14)$$

where  $Q$  is the canonical partition function, and  $\Omega(\psi)$  is the configuration density function. As we postulate that  $\mathbf{E}$  characterizes a microstate, equal *a priori* probability leads to

$$\Omega(\psi)d\psi = d\mathbf{E} = \frac{\pi}{2}d\psi, \quad Q = \int_V \exp(-\beta\psi(\mathbf{E}))d\mathbf{E} = \frac{\pi}{2\beta}, \quad (15)$$



where  $V := \{\mathbf{E} \in \mathbb{R}_{\text{sym}}^{2 \times 2} : \text{Tr} \mathbf{E} = 0\}$ . In other words,  $\Omega(\psi)$  is constant, and our observations are consistent with a canonical ensemble. In addition, the tests by Dean and Lefèvre [18] and McNamara *et al.* [54] become trivial: the ratio of two overlapping exponential distributions will necessarily give another exponential distribution. Further rudimentary calculations follow. The ensemble-averaged energy and entropy are

$$\langle \psi \rangle = -\frac{d \ln Q}{d\beta} = T, \quad \langle s \rangle = \ln Q + \beta \langle \psi \rangle = 1 + \ln \frac{\pi T}{2}, \quad (16)$$

respectively. Indeed  $T = d \langle \psi \rangle / d \langle s \rangle$ . We will henceforth term this temperature the E2 (E-square) temperature for planar polygonal tessellation.

Similar to the volume function in granular assembly by Blumenfeld and Edwards [10], the trace-free tensor  $\mathbf{E}$  resides in a particularly small, two-dimensional phase space, which results in the constancy of  $\Omega$  and the particularly simple behavior of  $\psi$ . A useful prediction is that if we extend the theory to space partitions in three dimensions,  $\mathbf{E}$  will instead reside in a 5-dimensional phase space, and we expect

$$\Omega^{3D}(\psi) \propto \psi^{3/2}. \quad (17)$$

This prediction will be validated in studying three-dimensional space partitions in future work, and the E2 temperature may be properly generalized to higher and arbitrary dimensions.

The physical meaning of  $\mathbf{E}$  is self-evident: it represents deformation, and hence is typically associated with energy in one form or another. In the wide range of phenomena we studied, the constitutive relations come in different forms (some are yet unknown). However, a couple of usual possibilities can be speculated. If the energy is bulk-elastic in nature, then any physically reasonable elastic model of a polygon, valid in the small-to-moderate deformation regime, *must* follow the form [33]

$$\Delta \Psi = \mu |\mathbf{E}|^2, \quad (18)$$

where  $\mu$  is the first Lamé constant, whereas the second constant is not needed as  $\text{Tr} \mathbf{E} = 0$  (SI). On the other hand, if energy is associated with edge lengths or perimeters, such as in the case of models for 2D confluent tissues [9, 41, 51], Eq. (18) is still a formally valid approximation, as the change in perimeter is also proportional to  $|\mathbf{E}|^2$  in leading-order approximation (SI). These two possibilities of linear constitutive relation cover a reasonably wide range of physical systems, although they do not apply to certain scenarios such as granular assembly and convection patterns. The conservational laws in these latter systems in relation to the deformation strain await further exploration.

In relations to the above point, we have thus far demonstrated a consistency with the canonical ensemble. Further specific details depend on identifying the conservation principles in each system, namely, the conservation of a energy or pseudo-energy. Nevertheless, if we were to temporarily accept applicability of the ensemble theory, in light of the ensemble averages (16) Fig. 3b becomes particularly interesting: we effectively demonstrated a phase space of  $(p_0, \langle s \rangle)$  as  $\langle s \rangle \propto \ln T$ .

We have thus presented a two-fold story in this work: *i*) that the Boltzmann-like distribution in the squared deformation tensor norm leads to the  $k$ -Gamma distributions in the aspect ratio; *ii*) that both types of distributions are universal in a wide variety of planar tessellations spanning different physical

systems. Although these two distributions are mutually deducible, the simpler (the Boltzmann-like) is frequently the more fundamental. The E2 temperature is well-defined, and can be generalized to higher dimensions. When all data sets are compiled in a phase space, a surprising result emerges that the value  $p_0^*$  seems to be broadly applicable as a threshold to separate regimes (“phases”) of behavior.

The mean-field strain tensor, with its clear physical and geometric meaning, is an ideal quantity connecting the conservation principles, the energy (or pseudo-energy) landscape, and the geometric distributions. Since the landmark proposal of the Kelvin structure in 1887 [79], networks that partition the space have been of both significance and grave challenges due to their complexities. Global minimization of surface areas and/or energies in these networks is intrinsically difficult due to non-convexity, and metastable states are believed to prevail. In three dimensions only a counter-example was offered [82], whereas in the two dimensions, the Honeycomb Conjecture was proven only recently by Thomas Hales [35] - the honeycomb structure as the “optimal” structure corresponds precisely to the absolute zero of the E2 temperature. This zero temperature is however not uniquely defined - repeating triangular and square patterns are other possibilities. Nevertheless, conjunction with other intensive parameters such as the preferred perimeter leads to an attractive path of establishing a thermodynamic framework, especially considering that both parameters are geometric in nature, and transcend differences in physical mechanisms. This framework promises to describe generally polygonal and polyhedron networks randomized by active agitations, structural defects, and noises, among others.

## Author contributions

HL, LL, and KDI designed the research; LL and HL developed the theory; RL, ZZ, and CI analyzed images; HL and RL analyzed data; CI and ZZ performed experiments; HL, LL, and KDI wrote the paper.

## Acknowledgement

The authors are grateful to Dr. Yuanwang Pan for providing fixed wing disc images in the Drosophila Fix group. The authors acknowledge helpful discussions with Dr. Troy Shinbrot, and funding support from NIH R21 CA220202-02 (PI: HL); NSF CMMI 1351561 and DMS 1410273 (PI: LL); and NIH R35 GM131748 (PI: KDI).

## Competing interests

The authors declare no competing interests.

## Data availability

The datasets generated during and/or analysed during the current study are available from the corresponding authors on reasonable request.

## Methods

### Data Collection

Among the data groups listed in Table 1, the last 3 (Droso Fix, Droso Live, and MDCK) are generated from this work, whereas other data types are collected from the public domain. They are briefly described below, and the specific images analyzed are identified in the references where possible.

**Bénard-Marangoni Convection (Bénard)** Bénard-Marangoni convection patterns from experimental images published in journal papers, books, and online image [11, 14, 20, 22, 26, 74].

**Granular Packing (Gran-exp and Gran-sim)** Images are adapted from research papers, including both experimental [6, 12, 85] and simulation work [4, 29, 44, 45, 56, 57, 63]. While elements in packing are typically not polygonal, the polygonal tessellation we analyze derives from their Voronoi volumes.

**Salt Flat of Uyuni (Salt Flat)** All images of the Salar de Uyuni (Bolivia) are from online, or captured from still frames of online videos. Credits are given to identifiable author IDs, and time stamps in videos are provided [27, 28, 31, 52, 55, 60, 76].

**Landforms on Mars (Mars)** All photos come from the High Resolution Imaging Science Experiment (HiRISE) on board the Mars Reconnaissance Orbiter and are produced by NASA, JPL-CalTech and University of Arizona [47, 50, 65, 66, 67, 77]. The mechanisms of geological pattern formation on Mars are still the subject of active studies, and theories include desiccation [50], thermal contraction [47, 65, 66], and ice sublimation [77]. The image from [67] likely indicates ridges of sand dunes.

**Veins on Leaves (Leaves)** All images are from online where proper credits are given to website, author, or author ID whichever is identifiable [16, 32, 40, 42, 69, 78]. Species are not identified in photos except for [16], which shows *Ficus lyrata* (Fiddle-Leaf Fig).

**Landforms in the Arctic (Arctic)** Polygonal landforms in or near the Arctic are mostly ice wedges [2, 7, 48, 61, 71, 72, 83] or tundra [17, 53], whereas patterns in the latter typically corroborate with locations of ice wedges, too.

**Supergranulation on Solar Surface (Solar)** Supergranulation patterns on the solar surface from observations [8, 15, 19, 34, 37, 75].

**Cracked dry earth (Cracks)** Land cracks, mostly probably formed due to desiccation. Images are collected from the internet [1, 13, 39, 43, 46, 58, 70, 81, 86].

**Drosophila wing disc, fixed (Droso Fix)** Drosophila were cultured at 25°C. To obtain fixed wing discs at different stages, eggs were laid for 2 to 4h, and larvae were dissected at 72, 84, 96, 108 and 120h after egg laying (AEL). Dissected wing discs were fixed in 4% paraformaldehyde for 15 min at room

temperature. Staining of fixed wing discs was performed essentially as described in [68] using rat anti-E-cad (1:400 DCAD2; DSHB) and anti-rat Alexa Fluor 647 (Jackson ImmunoResearch, 712-605-153). Images were captured on a Leica SP8 confocal microscope. To compensate for aberrations due to the curvature of wing disc and signals from the peripodial epithelium, we used the Matlab toolbox ImSAnE [36] to detect and isolate a slice of the wing disc epithelium surrounding the adherens junctions, which was then projected into a flat plane, as described previously [62].

**Drosophila wing disc, live (Droso Live)** For live imaging of cultured wing discs, larvae expressing GFP-labelled E-cadherin from a Ubi-Ecad:GFP transgene were dissected at 96h AEL, and then cultured based on the procedure of Dye *et al.* [21]. Live wing discs were imaged using a Perkin Elmer Ultraview spinning disc confocal microscope every 8 mins for 12 hours.

**Plated MDCKIIG cells (MDCK)** MDCKIIG (a gift from W. James Nelson, Stanford University) cells were cultured in low-glucose Dubecco’s modified Eagle’s medium (DMEM) (Life Technologies) supplemented with 10% fetal bovine serum (FBS) and antibiotic-antimycotic. Cells were used at low passage number, checked regularly for contamination by cell morphology and mycoplasma testing. Cells were plated at different densities (1.5, 3, 4.5, 6, and  $7.5 \times 10^4$  cells/cm<sup>2</sup>) on coverslips coated with 0.6 mg/ml of collagen for 15 min at room temperature and washed with PBS. After 48 hours, cells were fixed with 4% paraformaldehyde in PBS++ (phosphate- buffered saline supplemented with 100 mM MgCl<sub>2</sub> and 50 mM CaCl<sub>2</sub>) for 10 min at room temperature. Immunostaining was performed as in Ibar *et al.* using mouse anti-ZO1 (1:1000, Life Technologies #33-9100) and anti-mouse Alexa Fluor 647 (Jackson ImmunoResearch) [38]. Images were acquired using LAS X software on a Leica TCS SP8 confocal microscope system using a HC PL APO 63×/1.40 objective.

## Image and data analysis

Fluorescent images are analyzed using Tissue Analyzer, a plug-in of ImageJ (version 1.52j), from which the cells are sectioned and cell centroids, edges, and vertices are identified. Post-processing is then performed with MATLAB. For each cell, the second area moment tensor, defined with respect to the cell centroid  $\mathbf{c}$ , is

$$\mathbf{M} = \int_{\mathcal{P}} (\mathbf{y} - \mathbf{c}) \otimes (\mathbf{y} - \mathbf{c}) dA, \quad (19)$$

where the integration is over the polygon (cell)  $\mathcal{P}$ . Note that here we ignore the curvature of cell edges and assume (by approximation) that they are straight lines connecting vertices. Standard and exact formulae are available for polygons which we use to compute the components of  $\mathbf{M}$  with only the coordinates of the vertices,  $\mathbf{y}_j$ ’s. The aspect ratio  $a_r$  is

$$a_r = \sqrt{\frac{\max(\lambda_1, \lambda_2)}{\min(\lambda_1, \lambda_2)}},$$

where  $\lambda_1$  and  $\lambda_2$  are eigenvalues of  $\mathbf{M}$ .

The mean-field deformation tensor  $\mathbf{F}$  can be approximated via several different approaches, one of them being minimizing the residue of Eq. (3) in the sense of least square. The strain tensor  $\mathbf{E}$  can then be computed accordingly. However, the most convenient and consistent manner of obtaining  $\mathbf{E}$  in the current

context is via  $\mathbf{M}$  itself,

$$\mathbf{E}' = \left( \frac{\mathbf{M}}{\sqrt{\det \mathbf{M}}} \right)^{\frac{1}{2}} - \mathbf{I}, \quad \mathbf{E} = \mathbf{E}' - (\text{Tr} \mathbf{E}') \mathbf{I} / 2,$$

which bypasses the calculation of  $\mathbf{F}$ .

The coefficient of determination,  $R^2$ , follows the standard definition,

$$R^2 = 1 - \frac{\text{var}(\mathbf{f} - \mathbf{f}')}{\text{var}(\mathbf{f})}.$$

Here 'var' denotes variance,  $\mathbf{f}$  is the data presented in array form, and  $\mathbf{f}'$  is the corresponding array generated via fitting (such as for  $|\mathbf{E}|^2$ ) or a theoretical prediction (such as for  $a_r$ ).

## References

- [1] 3dshtamp (author ID). Online image: White or light gray brick texture. [URL: <https://www.shutterstock.com/image-illustration/white-light-gray-brick-texture-765044275>].
- [2] The International Permafrost Association. Online image: Permafrost polygon. [URL: <https://ipa.arcticportal.org/products/mediamenu/galleries/category/1-permafrost-impressions>].
- [3] L. Atia, D. Bi, Y. Sharma, J. A. Mitchel, B. Gweon, S. A. Koehler, S. J. DeCamp, B. Lan, J. H. Kim, R. Hirsch, A. F. Pegoraro, K. H. Lee, J. R. Starr, D. A. Weitz, A. C. Martin, J.-A. Park, J. P. Butler, and J. J. Fredberg. Geometrical constraints during epithelial jamming. *Nat. Phys.*, 14:613–620, 2018.
- [4] E. Azéma, F. Radjai, R. Peyroux, and G. Saussine. Force transmission in a packing of pentagonal particles, figure 2(a). *Phys. Rev. E*, 76(1):011301, 2007.
- [5] D. Barthès-Biesel and H. Sgaier. Role of membrane viscosity in the orientation and deformation of a spherical capsule suspended in simple shear flow. *J. Fluid Mech.*, 160:119–135, 1985.
- [6] R. P. Behringer. Online presentation: Useful slides from granular experiment for DARPA, page 40. [URL: <https://www.phy.duke.edu/~bob/160916darpa.ppt>].
- [7] C. Bernard-Grand’Maison and W. Pollard. An estimate of ice wedge volume for a High Arctic polar desert environment, Fosheim Peninsula, Ellesmere Island, figure 4 top right panel. *Cryosphere*, 12(11):3589–3604, 2018.
- [8] F. Berrilli, I. Ermolli, A. Florio, and E. Pietropaolo. Average properties and temporal variations of the geometry of solar network cells, figure 1 right panel. *Astron. Astrophys.*, 344:965–972, 1999.
- [9] D. Bi, J. H. Lopez, J. M. Schwarz, and M. L. Manning. A density-independent rigidity transition in biological tissues. *Nat. Phys.*, 11:1074–1079, 2015.
- [10] R. Blumenfeld and S. F. Edwards. Granular entropy: Explicit calculations for planar assemblies. *Phys. Rev. Lett.*, 90(11):114303, 2003.
- [11] T. Boeck. *Coherent structures, instabilities, and turbulence in interfacial and magnetohydrodynamic flows*, figure 1(b). PhD thesis, Technische Universität Ilmenau, 2010.
- [12] D. Buscombe and D. M. Rubin. Advances in the simulation and automated measurement of well-sorted granular material: 1. Simulation, figure 3. *J. Geophys. Res. Earth Surf.*, 117(F2), 2012.
- [13] calling wisdom (author ID). Online image: Cracked land, June 2009. [URL: <http://www.nipic.com/show/2/8/ee5e32f449b1c4e7.html>].
- [14] P. Cerisier, S. Rahal, and N. Rivier. Topological correlations in Bénard-Marangoni convective structures, figure 1. *Phys. Rev. E*, 54(5):5086–5094, 1996.
- [15] S. Chatterjee, S. Mandal, and D. Banerjee. Variation of supergranule parameters with solar cycles: Results from century-long Kodaikanal digitized Ca II K data, figure 1(d). *Astrophys. J.*, 841(2):70 (10pp), 2017.

- [16] D. Clode. Online image: *Ficus lyrata* leaf, October 2012. [URL: <https://reforestation.me/flower-photos-1/>].
- [17] F. Cresto-Aleina. *Scale interactions in high-latitude ecosystems*, figure 2.1. PhD thesis, Max Planck Institute for Meteorology, 2014.
- [18] D. S. Dean and A. Lefèvre. Possible test of the thermodynamic approach to granular media. *Phys. Rev. Lett.*, 90(19):198301, 2003.
- [19] M. L. DeRosa and J. Toomre. Evolution of solar supergranulation, figure 7(a). *Astrophys. J.*, 616(2):1242–1260, 2004.
- [20] P. G. Drazin. *Introduction to hydrodynamic stability*, chapter 6, pages 94, figure 6.2. Cambridge University Press, 2002.
- [21] N. A. Dye, M. Popović, S. Spann, R. Etournay, D. Kainmüller, S. Ghosh, E. W. Myers, F. Jülicher, and S. Eaton. Cell dynamics underlying oriented growth of the drosophila wing imaginal disc. *Development*, 144:4406–4421, 2017.
- [22] M. Van Dyke. *An album of fluid motion*, chapter 5, pages 83, figure 142. The Parabolic Press, Stanford, CA, 1982.
- [23] S. F. Edwards and D. V. Grinev. Statistical mechanics of vibration-induced compaction of powders. *Phys. Rev. E*, 58:4758, 1998.
- [24] S. F. Edwards and R. B. S. Oakeshott. Theory of powders. *Physica A*, 157:1080–1090, 1989.
- [25] R. Farhadifar, J. Röper, B. Aigouy, S. Eaton, and F. Jülicher. The influence of cell mechanics, cell-cell interactions, and proliferation on epithelial packing. *Curr. Biol.*, 17:2095–2104, 2007.
- [26] Fluid Dynamics (author ID). Online video: Bénard-Marangoni instability, t=207 s, December 2016. [URL: <https://www.youtube.com/watch?v=v2vMXmuC818>].
- [27] Fly around the world (author ID). Online video: Travel the world, Uyuni vol1, Bolivia by drone (Phantom), t=101 s, February 2016. [URL: <https://www.youtube.com/watch?v=GSYLH462Nis>].
- [28] Flying The Nest (author ID). Online video: Bolivia salt flats, Salar de Uyuni, worlds largest mirror, t=493 s, November 2017. [URL: [https://www.youtube.com/watch?v=V\\_RFDqrJC9U&t=493s](https://www.youtube.com/watch?v=V_RFDqrJC9U&t=493s)].
- [29] G. Frenkel, R. Blumenfeld, M. Blunt, and P. King. Online presentation: Topological analysis of packings: Application to flow properties in granular porous media, page 16. [URL: <https://slideplayer.com/slide/6928905/>].
- [30] S. Garcia, E. Hannezo, J. Elgeti, J.-F. Joanny, P. Silberzan, and N. S. Gov. Physics of active jamming during collective cellular motion in a monolayer. *Proc. Natl. Acad. Sci. USA*, 112:15314–15319, 2015.
- [31] gffandre (author ID). Online image: Salar de Uyuni, February 2018. [URL: <http://www.dronestagr.am/salar-de-uyuni/>].

- [32] gitan100 (author ID). Online image: Vector leaf veins seamless texture. [URL: <https://www.shutterstock.com/zh/image-vector/vector-leaf-veins-seamless-texture-98150471?src=HUAi-C5Hv27glBnNFx2Y4Q-1-41>].
- [33] M. E. Gurtin, E. Fried, and L. Anand. *The Mechanics and Thermodynamics of Continua*. Cambridge University Press, 2010.
- [34] H. J. Hagenaar and C. J. Schrijver. The distribution of cell sizes of the solar chromospheric network, figure 3 lower panel. *Astrophys. J.*, 481(2):988–995, 1997.
- [35] T. C. Hales. The honeycomb conjecture. *Discrete & Computational Geometry*, 25(1):1–22, 2001.
- [36] I. Heemskerk and S. J. Streichan. Tissue cartography: compressing bio-image data by dimensional reduction. *Nat. Methods*, 12:1139–1142, 2015.
- [37] J. Hirzberger, L. Gizon, S. K. Solanki, and T. L. Duvall. Structure and evolution of supergranulation from local helioseismology, figure 7. In L. Gizon, P. S. Cally, and J. Leibacher, editors, *Helioseismology, asteroseismology and MHD connections*, pages 415–435. Springer, New York, 2008.
- [38] C. Ibar, E. Kirichenko, B. Keepers, E. Enners, K. Fleisch, and K. D. Irvine. Tension-dependent regulation of mammalian Hippo signaling through LIMD1. *J. Cell Sci.*, 131(5):jcs214700, 2018.
- [39] Inspired Boy (author ID). Online image: Surface crack material [PSD], October 2015. [URL: <http://inspiredboy.com/surface-crack-material/>].
- [40] J. W. Kimball. Online image: The leaf, January 2012. [URL: <http://www.biology-pages.info/L/Leaf.html>].
- [41] S. Kim and S. Hilgenfeldt. Cell shapes and patterns as quantitative indicators of tissue stress in the plant epidermis. *Soft Matter*, 11:7270–7275, 2015.
- [42] N. Kinnear. Online image: Leaf lines V, September 2011. [URL: <https://fineartamerica.com/featured/leaf-lines-v-natalie-kinnear.html>].
- [43] Kojihirano (author ID). Online image: Dry lake bed texture. [URL: <https://www.dreamstime.com/stock-photo-dry-lake-bed-texture-crackled-earth-racetrack-death-valley-national-park-california-image41139404>].
- [44] L. Kovalcinova, A. Goulet, and L. Kondic. Percolation and jamming transitions in particulate systems with and without cohesion, figure 1(a). *Phys. Rev. E*, 92(3):032204, 2015.
- [45] N. W. Krapf. Force propagation in isostatic granular packs, figure 9 left panel. *Phys. Rev. E*, 86(2):021302, 2012.
- [46] kzww (author ID). Online image: Cracked dry earth. [URL: <https://www.shutterstock.com/image-photo/cracked-dry-earth-abstract-background-1142812457>].



- [47] J. Levy, J. Head, and D. Marchant. Thermal contraction crack polygons on Mars: Classification, distribution, and climate implications from HiRISE observations, figure 2(b), 7(b), 8(a) and (b). *J. Geophys. Res. Planets*, 114(E1), 2009.
- [48] A. K. Liljedahl, J. Boike, R. P. Daanen, A. N. Fedorov, G. V. Frost, G. Grosse, L. D. Hinzman, Y. Iijma, J. C. Jorgenson, N. Matveyeva, M. Necsoiu, M. K. Reynolds, V. E. Romanovsky, J. Schulla, K. D. Tape, D. A. Walker, C. J. Wilson, H. Yabuki, and D. Zona. Pan-Arctic ice-wedge degradation in warming permafrost and its influence on tundra hydrology, figure 3(a) and (b), middle panel. *Nat. Geosci.*, 9(1):312–318, 2016.
- [49] A. J. Liu and S. R. Nagel. Jamming is not just cool any more. *Nature*, 396:21–22, 1998.
- [50] M. R. El Maarry, W. J. Markiewicz, M. T. Mellon, W. Goetz, J. M. Dohm, and A. Pack. Crater floor polygons: Desiccation patterns of ancient lakes on Mars, figure 12 right panel. *J. Geophys. Res. Planets*, 115(E10), 2010.
- [51] M. L. Manning, R. A. Foty, M. S. Steinberg, and E.-M. Schoetz. Coaction of intercellular adhesion and cortical tension specifies tissue surface tension. *Proc. Natl. Acad. Sci. USA*, 107(28):12517–12522, 2010.
- [52] J. Martinez. Online video: Trailer San Pedro - Uyuni 2017 drone view, t=23 s, September 2017. [URL: <https://www.youtube.com/watch?v=tqX3dYHGF8g&t=23s>].
- [53] N. Matt. Online image: Science in the 1002 area. Fodar News, February 2019. [URL: <http://fairbanksfodar.com/science-in-the-1002-area>].
- [54] S. McNamara, P. Richard, S. Kiesgen de Richter, G. Le Caër, and R. Delannay. Measurement of granular entropy. *Phys. Rev. E*, 80(3):031301, 3009.
- [55] Mika world tour (author ID). Online video: Voyage au Salar de Uyuni, t=127s, January 2017. [URL: <https://www.youtube.com/watch?v=u291MNVpRIM&t=127s>].
- [56] G. Mollon and J. Zhao. Fourier–Voronoi–based generation of realistic samples for discrete modelling of granular materials, figure 11 top panel. *Granul. Matter*, 14(5):621–638, 2012.
- [57] G. Mollon and J. Zhao. Realistic generation and packing of dem sand samples, figure 5(a1). In *Advances in Civil, Environmental and Materials Research ACEM*, August 2012.
- [58] T. Mongkolsin. Online image: Soil texture crack background. [URL: [https://www.123rf.com/photo\\_31964240\\_soil-texture-crack-background.html?fromid=VTRRbBHIHQW1qWVRmbzFYWEwxSjZxUT09](https://www.123rf.com/photo_31964240_soil-texture-crack-background.html?fromid=VTRRbBHIHQW1qWVRmbzFYWEwxSjZxUT09)].
- [59] K. D. Nnetu, M. Knorr, S. Pawlizak, T. Fuhs, and J. A. Kas. Slow and anomalous dynamics of an MCF-10A epithelial cell monolayer. *Soft Matter*, 9:9335–9341, 2013.
- [60] North Branch (author ID). Online video: Uyuni salt flats (Salar de Uyuni) drone, Potosi - Bolivia, t=85 s, September 2017. [URL: <https://www.youtube.com/watch?v=CbVGic9GQR4&t=85s>].

- [61] The Arctic Research Consortium of the United States. Online image: Landscape change in the tundra: Citizen-scientist driven arctic observations, 2018. [URL: <https://www.arcus.org/tac/projects/landscape-change>].
- [62] Y. Pan, I. Heemskerk, C. Ibar, B. I. Shraiman, and K. D. Irvine. Differential growth triggers mechanical feedback that elevates Hippo signaling. *Proc. Natl. Acad. Sci. USA*, 113:E6974–E6983, 2016.
- [63] L. Papadopoulos, J. G. Puckett, K. E. Daniels, and D. S. Bassett. Evolution of network architecture in a granular material under compression, figure 1(a). *Phys. Rev. E*, 97(3):032908, 2016.
- [64] J.-A. Park, J. H. Kim, D. Bi, J. A. Mitchel, N. T. Qazvini, K. Tantisira, C. Y. Park, M. McGill, S.-H. Kim, B. Gweon, J. Notbohm, R. Steward Jr, S. Burger, S. H. Randell, A. T. Kho, D. T. Tambe, C. Hardin, S. A. Shore, E. Israel, D. A. Weitz, D. J. Tschumperlin, E. P. Henske, S. T. Weiss, M. L. Manning, J. P. Butler, J. M. Drazen, and J. J. Fredberg. Jamming and cell shape in the asthmatic airway epithelium. *Nat. Mater.*, 14:1040–1048, 2015.
- [65] The HiRISE Project. Online image: Polygonal patterned ground, February 2010. [URL: [https://www.uahirise.org/ESP\\_016641\\_2500](https://www.uahirise.org/ESP_016641_2500)].
- [66] The HiRISE Project. Online image: Polygonal patterned ground, April 2012. [URL: <https://mars.nasa.gov/resources/5314/polygonal-patterned-ground/>].
- [67] The HiRISE Project. Online image: Polygonal dunes, May 2013. [URL: <https://photojournal.jpl.nasa.gov/catalog/PIA17726>].
- [68] C. Rauskolb and K. D. Irvine. Localization of Hippo signaling components in *Drosophila* by fluorescence and immunofluorescence. In A. Hergovich, editor, *Methods in Molecular Biology, Vol. 1893: The Hippo pathway*, pages 61–73. Humana Press, 2018.
- [69] rclassenlayouts (author ID). Online image: Leaf vein. [URL: [https://www.123rf.com/photo\\_19683272\\_leaf-vein-veins-branched-network-photosynthesis-spring-green-leaf-surface-texture.html](https://www.123rf.com/photo_19683272_leaf-vein-veins-branched-network-photosynthesis-spring-green-leaf-surface-texture.html)].
- [70] Releon8211 (author ID). Online image: Dried and cracked ground. [URL: <https://www.dreamstime.com/stock-photo-dried-cracked-ground-general-illustration-image56453384>].
- [71] D. Ronald. Online image: High centered orthogonal ice wedge polygons in northern Canadian archipelago, November 2009. [URL: <http://permafrost.gi.alaska.edu/photos/image/80>].
- [72] S. Matthew. Online image: Ivotuk polygons. [URL: <https://www.erd.usace.army.mil/Media/Images/igphoto/2000725201/>].
- [73] M. Sadati, N. T. Qazvini, R. Krishnan, C. Y. Park, and J. J. Fredberg. Collective cell migration and cell jamming. *Differentiation*, 86(3):121–125, 2013.

- [74] M. F. Schatz, S. J. VanHook, W. D. McCormick, J. B. Swift, and H. L. Swinney. Time-independent square patterns in surface-tension-driven Bénard convection, figure 2(b), 4(a), (b), and (d). *Phys. Fluids*, 11(9):2577–2582, 1999.
- [75] C. J. Schrijver and H. J. Hagenaar. On the patterns of the solar granulation and supergranulation, figure 2. *Astrophys. J.*, 475(1):328–337, 1997.
- [76] Sergeo540 (author ID). Online video: Bolivia Sucre Salar de Uyuni cinematic travel video 4K, t=163 s, January 2019. [URL: <https://www.youtube.com/watch?v=Ha7twopCwHw&t=163s>].
- [77] R. J. Soare, S. J. Conway, L. E. McKeown, E. Godin, and J. Hawksell. Possible ice-wedge polygons in Utopia Planitia, Mars, and their poleward latitudinal-gradient, figure 4. In *50th Lunar and Planetary Science Conference*, volume 50, March 2019.
- [78] SuradechK (author ID). Online image: Leaf-texture abstract background with closeup view on leaf veins. [URL: <https://www.canstockphoto.ca/leaf-texture-abstract-background-with-38163721.html>].
- [79] W. Thomson. LXIII. On the division of space with minimum partitional area. *The London, Edinburgh, and Dublin Philosophical Magazine and Journal of Science*, 24(151):503–514, 1887.
- [80] V. Trappe, V. Prasad, L. Cipelletti, P. N. Segre, and D. A. Weitz. Jamming phase diagram for attractive particles. *Nature*, 411:772–775, 2001.
- [81] Y. Wang, D. Feng, and C. W. Ng. Modeling the 3D crack network and anisotropic permeability of saturated cracked soil, figure 1. *Comput. Geotech.*, 52:63–70, 2013.
- [82] D. Weaire and R. Phelan. A counter-example to Kelvin’s conjecture on minimal surfaces. *Philosophical Magazine Letters*, 69(2):107–110, 1994.
- [83] P. Worsley. Ice-wedge growth and casting in a Late Pleistocene periglacial, fluvial succession at Baston, Lincolnshire, figure 5. *Mercian Geol.*, 18(3):159–170, 2014.
- [84] M. Yu, R. B. Lira, K. A. Riske, R. Dimova, and H. Lin. Ellipsoidal relaxation of deformed vesicles. *Phys. Rev. Lett.*, 115:128303, 2015.
- [85] S. C. Zhao, S. Sidle, H. L. Swinney, and M. Schröter. Correlation between Voronoi volumes in disc packings, figure 2(a). *EPL*, 97(3):34004, 2012.
- [86] Zhaojiankang (author ID). Online image: Tierra secada y agrietada. [URL: <https://es.dreamstime.com/imagen-de-archivo-libre-de-regal%C3%ADas-tierra-secada-y-agrietada-image39145796>].